JOURNAL OF GEOPHYSICAL RESEARCH, VOL. 103, NO. A11, PAGES 26,323–26,335, NOVEMBER 1, 1998

UARS observations of Birkeland currents and Joule heating rates for the November 4, 1993, storm

B. J. Anderson, J. B. Gary,[1] and T. A. Potemra[2]

Applied Physics Laboratory, Johns Hopkins University, Laurel, Maryland

R. A. Frahm, J. R. Sharber, and J. D. Winningham

Southwest Research Institute, San Antonio, Texas

Abstract. Magnetic field and particle observations from the Upper Atmosphere Research Satellite particle environment monitor (UARS/PEM) are used to estimate field-aligned currents, electron precipitation energy flux, ionospheric conductivities, and Joule heating rates during the main phase of the November 4, 1993, geomagnetic storm. From 0300 to 1200 UT on November 4 the auroral oval expanded equatorward of 65° magnetic latitude (MLAT), and UARS encountered the polar cap on seven consecutive passes during the storm main phase. These passes provide data appropriate to determine field-aligned currents and estimate ionospheric Joule heating. For this storm, UARS sampled the midnight to dawn sector in the northern hemisphere and the noon to dusk sector in the southern hemisphere. The maximum net currents on the dayside and nightside are comparable and reach 1 A/m for several hours. The average Joule heating rates are comparable at midnight, early morning, and noon, where they are 9.2, 6.6, and 7.7 GW/h, respectively, but have a strong peak in the late afternoon, where they are 25.6 GW/h. In contrast, the electron precipitation energy deposition is highest near midnight at 5.6 GW/h but drops to less than half this level to 2.4 GW/h and 1.9 GW/h in the early morning and at dusk, respectively, but is very small near noon, only 0.24 GW/h. The Joule to particle energy deposition rate ratio thus varies by roughly an order of magnitude with local time, being over 40 near noon, about 20 at dusk, 3 near dawn, and 2 at midnight. The hemispherical Joule and electron precipitation heating rates, H_J and H_{elec}, are estimated to have been 290 GW and 50 GW, respectively, giving $H_J/H_{elec} = 4.5$ and $H_J + H_{elec} = 340$ GW. Differences between these averages and assimilative mapping of ionospheric dynamics (AMIE) results, $H_J = 200$ GW and $H_{elec} = 80$ GW, reflect time variability during the storm and are largely resolved when AMIE results only at the times of UARS passes are considered.

1. Introduction

The global energy input to regions of the high-latitude atmosphere provided by Joule dissipation of electric currents is thought to exceed the input due to energetic particle precipitation by about a factor of 3 [*Ahn et al.*, 1983; *Lu et al.*, 1996]. This disparity persists during major magnetic storms for which the Joule heating rate can surpass the solar EUV input at ionospheric altitudes [e.g., *Cooper et al.*, 1995]. The Birkeland field-aligned currents are a permanent feature of the auroral regions [cf. *Potemra*, 1994] whose intensity varies dramatically with geomagnetic activity. The total magnitudes of the Birkeland currents are typically 10^6 A but exceed 10×10^6 A during major magnetic storms [*Anderson et al.*, 1993]. The Birkeland currents are coupled by the horizontal Pedersen current which dissipates energy in the atmosphere by Joule heating. It is thought that the Joule dissipation should be of the order of 100 GW or more during major storms [*Foster et al.*, 1983; *Cooper et al.*, 1995; *Monreal Mac-Mahon and Gonzalez*, 1997], although estimating this rate from ground observation networks is difficult during highly disturbed periods because the auroral oval expands equatorward of the observation sites [e.g., *Feldstein et al.*, 1997].

Recent estimates of the total ionospheric Joule dissipation using assimilative mapping of ionospheric electrodynamics (AMIE) [*Richmond and Kamide*, 1988; *Lu et al.*, 1996] or empirical energetics relations [*Monreal Mac-Mahon and Gonzales*, 1997] rely primarily on ground-based or interplanetary magnetic field and plasma measurements, respectively, to infer the ionospheric electric field. Low-altitude satellite particle and drift meter data are also used in AMIE to supplement the model conductivities and electric field distributions inferred from ground magnetometer array data. The Joule dissipation is estimated using modeled ionospheric conductivities modified to account for particle precipitation in local times of low-altitude satellite overflights.

The particle environment monitor (PEM) on the Upper Atmosphere Research Satellite (UARS) is well suited for characterizing the field-aligned currents and particle-induced conductivities during disturbed conditions. The UARS orbit inclination is 57°, so the satellite reaches maximum magnetic latitudes of 65°N and 72°S and cuts through the auroral oval at four local times (two in each hemisphere) when the oval expands equatorward of 65° magnetic

[1]Now at Information Resource Department, University of Texas at Dallas, Richardson.

[2]Deceased, April 3, 1998.

Paper number 98JA01236.
0148-0227/98/98JA-01236$09.00.

latitude (MLAT). In addition, the accurate attitude knowledge provided by UARS yields the most precise low-altitude magnetic field measurements since the Magsat mission. The particle instrumentation provides coverage of precipitating electrons over the energies relevant for producing Pedersen and Hall ionospheric conductivities (see *Winningham et al.* [1993] for descriptions of the PEM instrumentation).

In this paper we use UARS/PEM data to estimate Joule heating and electron energy deposition during the main phase of the November 4, 1993, geomagnetic storm. Although this was a moderately intense storm, minimum *Dst* of −116 nT, the polar cap was observed below 65° MLAT for 6 hours during the storm main phase, and the Birkeland currents extended down to 52° MLAT. Using the PEM vector magnetometer (VMAG) we determined the Birkeland currents as described by *Anderson et al.* [1993] and used these to infer the corresponding ionospheric Pedersen currents. The medium energy particle spectrometer (MEPS) is used to measure electron precipitation and estimate the ionospheric height-integrated Pedersen conductivity under the satellite track. These data are combined to estimate the Joule heating rates and electron energy flux in four local time regimes, midnight, predawn, noon, and late afternoon, from which a global estimate of auroral zone thermospheric heating is obtained. This technique of combining magnetic field and precipitating electron data to estimate the Pedersen current, ionospheric conductivity, and Joule heating is essentially identical to that used by *Rich et al.* [1987, 1991]. The results are compared with recent determinations of storm-time energetics [e.g., *Lu et al.*, 1996; *Monreal Mac-Mahon and Gonzalez*, 1997] and indicate that analyses of the type presented here are important for reliably estimating Joule heating during storms. We find that the ratio between Joule and particle precipitation energy flux varies by an order of magnitude, from a minimum of near 2 at midnight to a maximum over 40 near noon. This variation is due primarily to a deep minimum in electron energy flux near noon.

2. Magnetic Field Observations

2.1. Auroral Zone Coverage Overview

Figure 1 shows the *Dst* profile for 10 days around the November 4, 1993, storm and an expanded view of the storm onset and main phase indicating the UARS MLAT coverage. This storm was associated with an *SI* and a *Dst* increase to +28 nT from 1500 to 1700 UT on November 3. The main phase began at about midnight on November 3, day 307. Storm recovery began about 1500 UT on November 4. (See *Knipp et al.* [this issue] for an overview of this storm.) The MLAT of UARS is shown in the bottom two panels of Figure 1, (top) north/nightside and (bottom) south/dayside. The dashed lines show the satellite MLAT and the bold lines indicate intervals during which UARS was in or poleward of the Birkeland currents. The sinusoidal 24-hour envelope reflects the rotation of the Earth's magnetic pole under the satellite orbit. UARS attained its maximum MLAT at about 0300 UT during the storm main phase and observed the equatorward expansion of the auroral oval beginning at 0100 UT on the dayside. The last UARS auroral observations for this period occurred just after 1200 UT on the dayside. On these and every intervening pass, UARS sampled the auroral zone.

2.2. Example Dayside and Nightside Passes

Figure 2 shows representative polar and stack plots of VMAG data for two auroral zone passes, one southern/dayside and one northern/nightside pass. The particle data for the nightside pass are discussed by *Sharber et al.* [this issue]. The coordinates used in the stack plots are NEP, where P is parallel to the background model field, E is eastward, and N is approximately northward. Both plots show views looking down from above the north magnetic pole (through the Earth for the southern hemisphere pass). The polar plots show the perturbation vector plotted along the satellite track and are useful for identifying regions of uniformly directed perturbations as well as rotations in the perturbations. The three line plots show the perturbation in each component for the pass. For this day, UARS attained its northernmost (southernmost) latitude at about 0200 (1400) MLT. These data and the particle data (not shown) indicate that the polar cap was encountered for about 1 min, from 0349:30 to 0350:30 UT at 1500 MLT during the dayside pass and for somewhat longer than 2 min, from 0930:00 to 0932:30 UT at about 0400 MLT, during the nightside pass. Although the local times at which the auroral currents were crossed varied slightly with the expansion of the oval, generally, the southern hemisphere passes crossed through the currents near noon and in the late afternoon. The northern hemisphere passes crossed near midnight and in the predawn hours.

The major features apparent in Figure 2 are as follows. On the dayside the region 1 and 2 currents are evident: region 2 from 0345 to 0347:30 and region 1 from 0347:30 to 0349:30 UT. The net ΔB is fairly large, over 1000 nT, whereas 300–500 nT is typical of moderately disturbed conditions [e.g., *Iijima and Potemra*, 1976]. We attribute the perturbation rotation near 1300 MLT, 0351 UT, to the cusp/mantle currents. On the nightside, the predawn region 1 and 2 signature, 0932 to 0933:30 UT, is smaller, ~500 nT, whereas strong, ~1000 nT, sunward perturbations were observed just postmidnight. The rotations near midnight, evident in the changing orientation of the perturbation vectors and also reflected in the sign reversals of BE from 0922 to 0925 UT, indicate 100 s of kilometer scale size structured currents often associated with surges. There were numerous substorms during this period and one just prior to this pass, onset occurring near 0910 UT [cf. *Sharber et al.*, this issue]. The general features of the magnetic perturbations, aside from variable vortical features on the nightside, were characteristic of all UARS passes that crossed into the polar cap.

The parallel perturbation signatures, negative/upward on the dayside and positive/upward on the nightside, indicate that the spacecraft moved poleward of an eastward (westward) Hall current on the dayside (nightside) associated with the electrojets but not very far over the sunward current associated with the polar cap Hall current. The position between the electrojet and polar cap Hall currents produces parallel perturbations in the sense observed, and these parallel perturbations are typical of UARS crossings into the polar cap [e.g., *Anderson et al.*, 1993].

2.3. Evaluation of Equivalent Pedersen Currents

One efficient way to quantitatively summarize the magnetic field observations is to consider the equivalent Pedersen current implied by the transverse (to **B**) perturbations, $\Delta\mathbf{B}_\perp$ [cf. *Rich et al.*, 1987]. To evaluate $\Delta\mathbf{B}_\perp$, the magnetic field data are first detrended by removing a model main field as described by *Anderson et al.* [1993]. We then identify the region of each pass over which Birkeland currents are observed and use the portions of each pass equatorward of the currents to detrend the data using a cubic polynomial fitted to the current-free end segments of each pass. This yields magnetic perturbations parallel $\Delta B_\parallel$ and perpendicular $\Delta\mathbf{B}_\perp$ to the model field. The vector $\Delta\mathbf{B}_\perp$ is then resolved into components along ΔB_a and across ΔB_c the spacecraft track. The across-track component

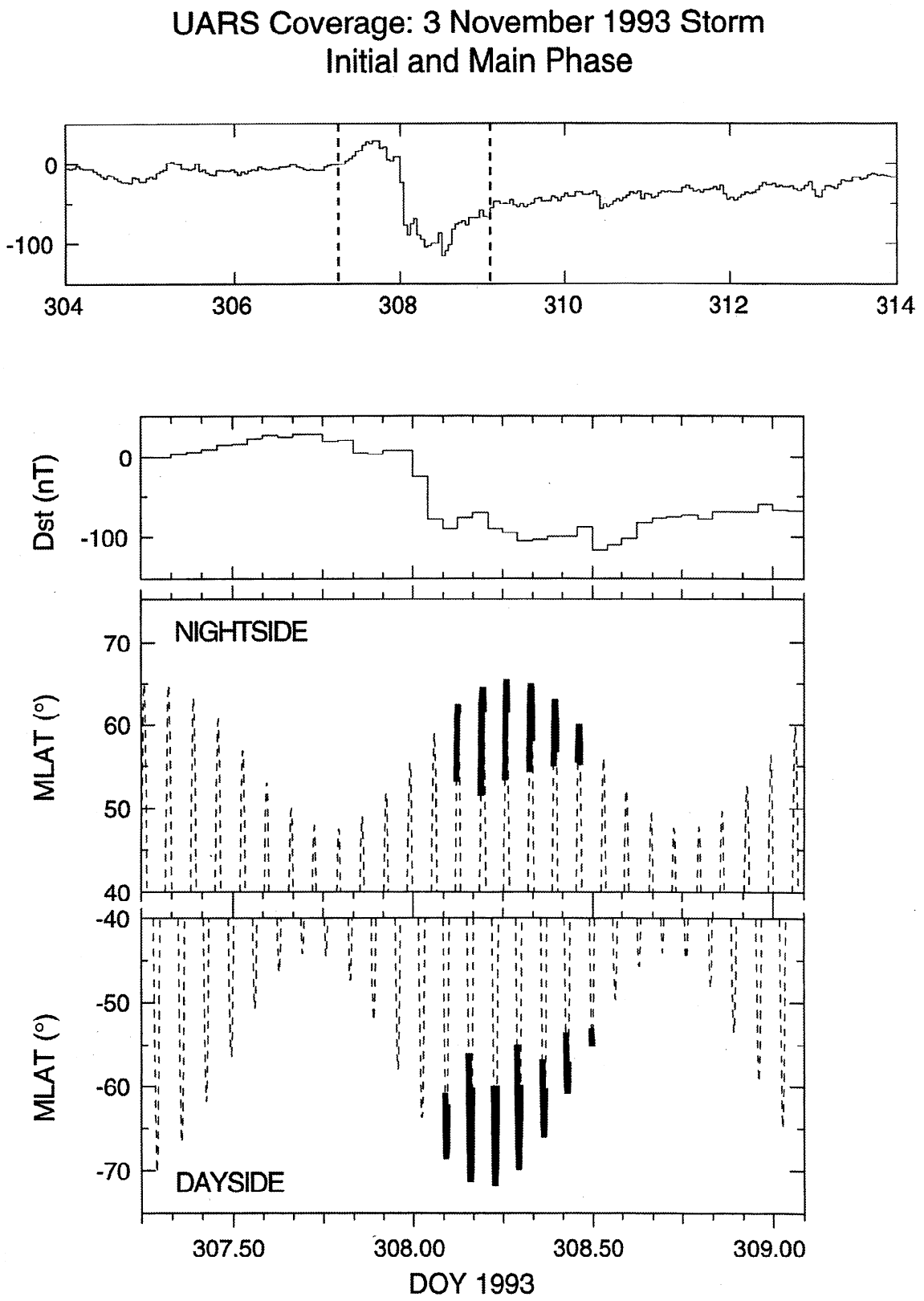

Figure 1. Overview of *Dst* and UARS auroral coverage for the November 4, 1993, day 308, storm. Top panel shows *Dst* for 10 days, 4 before and 6 after the storm main phase commencement. Vertical lines indicate the time range for the expanded view shown in the bottom panels. The UARS magnetic latitude is plotted as dashed lines. Bold solid lines indicate when UARS was poleward of the most equatorward field-aligned currents.

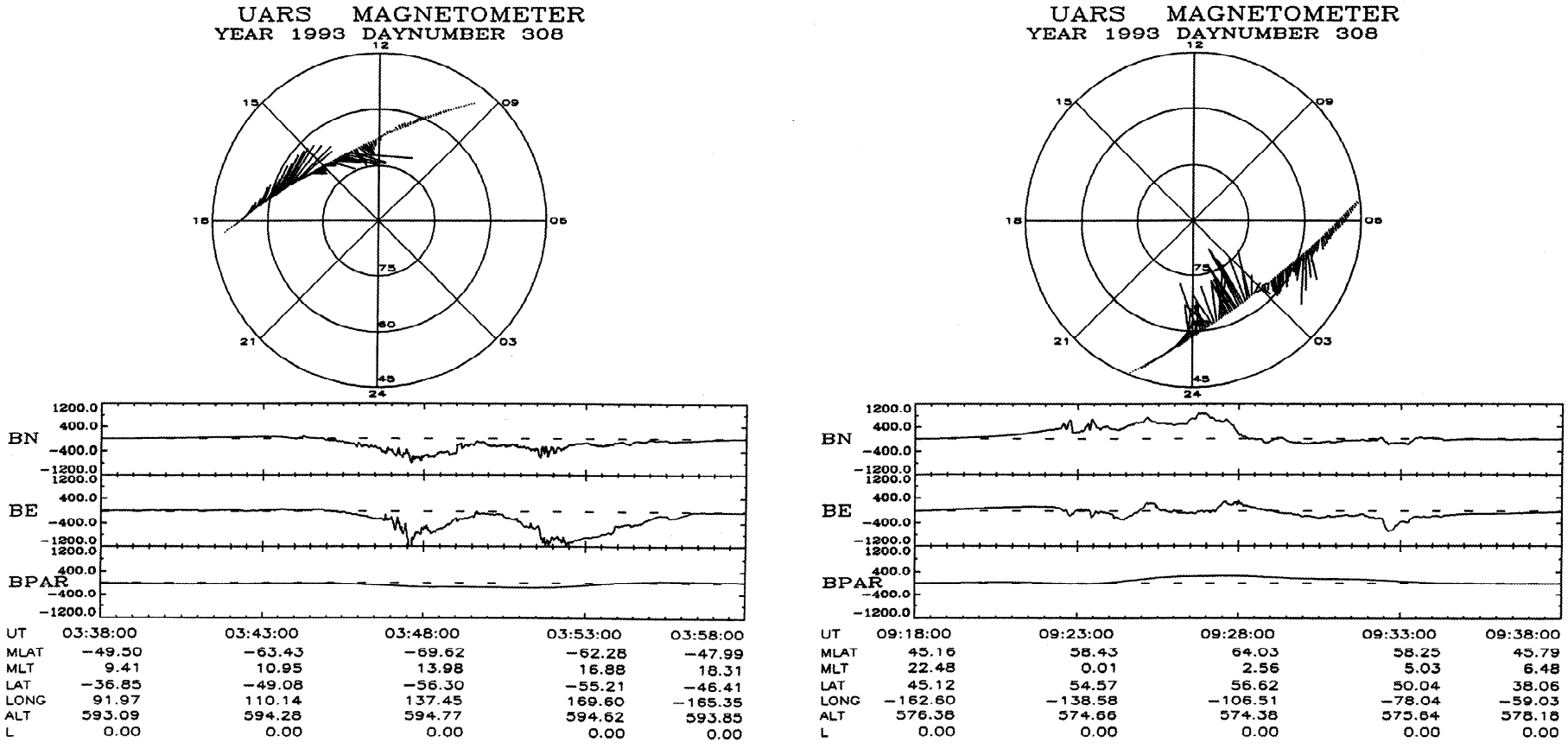

Figure 2. Magnetic field data for two auroral zone passes, over (left) the afternoon sector and (right) the morning sector. Polar plots show the perturbations transverse to the model magnetic field projected along the satellite track, and line plots show the northward, eastward, and poleward components of the magnetic perturbations.

is positive northward, that is, poleward (equatorward) in the northern (southern) hemisphere.

We used two methods to estimate the equivalent net current that the $\Delta\mathbf{B}_\perp$ perturbations represent. In method 1, we evaluated the minimum variance direction of the $\Delta\mathbf{B}_\perp$ for the center point of a 1-min sliding window. The minimum variance direction is taken to indicate the normal to the current sheet. The net current density is then estimated as the derivative of the across-track component, $d(\Delta B_c)/dx$, corrected for the angle θ between the current sheet normal and the satellite track. Here dx is the along-track distance increment. The perturbation that would have been observed for a crossing perpendicular to the current sheet is

$$\left(\frac{d(\Delta B_{tot})}{dx}\right)_1 = \left(\frac{d(\Delta B_c)}{dx}\right)\sqrt{1+\tan^2\theta} \quad (1)$$

To eliminate spurious results when the ΔB_c values are small, θ is restricted to the range ±60°. To determine the equivalent Pedersen current density, j_{net1}, one must adjust the ΔB observed at the UARS altitude, 585 km, to the ΔB that would be observed at the ionosphere, assumed to be 100 km. The ionospheric ΔB is higher by the factor $(r_{UARS}/r_i)^{3/2}$ where r_{UARS} and r_i are the geocentric radii of UARS and the ionosphere [cf. *Rich et al.*, 1987]. Thus j_{net1} is the integral of $(d(\Delta B_{tot})/dx)_1$ multiplied by $(r_{UARS}/r_i)^{3/2}/\mu_0 = 1.115 \times 7.96 \times 10^{-4}$ A m^{-1} nT^{-1}. To remove residual currents at the beginning and end of the pass, j_{net1} was detrended using a cubic polynomial fit to the segments of the pass on either end where no current flows. The sign of j_{net1} was determined by the sense of the across track perturbation derivative.

In method 2 we evaluated the derivative of both ΔB_c and ΔB_a to compute the total magnitude of the magnetic perturbation derivative, $(d(\Delta B_{tot}/dx))_2$. The sign of $(d(\Delta B_{tot}/dx))_2$ is the same as the sign of the across-track derivative, that is,

$$\left(\frac{d(\Delta B_{tot})}{dx}\right)_2 = \mathrm{sgn}\left(\frac{d(\Delta B_c)}{dx}\right)\sqrt{\left(\frac{d(\Delta B_c)}{dx}\right)^2 + \left(\frac{d(\Delta B_a)}{dx}\right)^2} \quad (2)$$

By including contributions from the along-track component in this way, method 2 approximately accounts for perturbations arising from non-sheet-like current forms. (Note, however, that the infinite current sheet approximation is implicit in equating the gradient of ΔB with a local current density.) The net current density j_{net2} was computed and detrended from $(d(\Delta B_{tot}/dx))_2$ as in method 1. Comparing methods 1 and 2 indicates how well the net current is measured.

This method for estimating the intensity of the ionospheric Pedersen current under the satellite track is nearly identical to that used by *Rich et al.* [1987]. One principal assumption in this approach is that the Birkeland current is due entirely to divergence of the Pedersen current. As discussed by *Rich et al.* [1987], this amounts to assuming that the ionospheric conductivities are uniform. By treating all magnetic perturbation gradients as currents, we also implicitly assume that the Birkeland currents are in the form of sheets. The primary differences in this analysis from that of *Rich et al.* [1987] are as follows: (1) By including a UARS specific main field model, we are able to reduce the variability of the baselines so that the polar cap perturbations are reliable and are not removed in the polynomial detrending procedure; and (2) the use of a sliding minimum variance analysis to estimate the current sheet orientation in method 1.

2.4. Storm Main Phase Equivalent Currents

Figure 3 shows stack plots of the equivalent Pedersen currents versus magnetic local time evaluated using method 1 for the series of (left) southern and (right) northern hemisphere auroral zone passes from 0025 to 1254 UT. In the southern hemisphere the best coverage is from 0340 UT to 0900 UT, during which there are four consecutive passes extending into the polar cap. On the nightside, there were three polar cap passes from 0740 UT to 1120 UT. The MLT coverage changes gradually during this period due to the eccentricity of the Earth's magnetic pole.

The large-scale structure of the currents on the dayside was consistent for the three passes from 0340 to 0715 UT: The maximum currents occurred from 1400 to 1800 MLT and were between 0.9 and 1.1 A/m, whereas near noon the maximum currents were typically 0.5 A/m. Although the currents observed on the 0833 UT pass were more structured, the same basic pattern was present. Typical active time currents have net magnetic perturbations of about 500 nT, 0.4 A/m and occasionally up to 1000 nT, 0.8 A/m [*Iijima and Potemra*, 1978], but during the largest storms the net $\Delta B_\perp$ can reach 1700 nT, 1.3 A/m [*Rich et al.*, 1990; *Fujii et al.*, 1992]. During the main phase of this storm the currents were consistently about twice those that typically occur during active periods but not quite as high as observed during the largest storms. The nightside currents tended to be more structured and were less consistent from pass to pass; compare the passes starting at 0425 UT, 0600 UT, and 0740 UT. The passes beginning at 0740 UT and 0915 UT were fairly similar, but the large positive current observed near the end of the 1055 UT pass was not present in either. Substorm intensifications were apparent during this period near 0730, 0815, 0845, 0910, 1030, and 1050 UT [cf. *Sharber et al.*, this issue], suggesting that the variable structures observed on the nightside were probably due to surges occurring at auroral breakup and moving away from midnight. The nightside currents occasionally reached 0.8 A/m but were typically less than about 0.6 A/m.

Given the consistent pattern of the currents and their magnitude, 0.5–1.0 A/m, one can estimate the total current. Taking the auroral oval to be at approximately 65° magnetic latitude, the circumference of the oval was about 17,000 km. Weighting the four local time sectors equally, the average net current was about 0.7 A/m giving a total current of roughly 11×10^6 A. It was sustained at about this value through most of the storm main phase. This is roughly twice the total current during typical substorm activity of about 5×10^6 A [*Iijima and Potemra*, 1978]. The AMIE result for the main phase of this storm gave net field-aligned currents of 6×10^6 A [*Knipp et al.*, this issue]. Restricting attention to times of the dayside UARS passes, however, the average AMIE result is 8.2×10^6 (B. Emery and D. Knipp, private communication, 1997). Part of the remaining difference may be due to the equatorward expansion of the oval, but considering the approximations used in extrapolating the total current from the UARS observations, we believe that this is not a serious discrepancy.

3. Particle and Joule Heating Estimates

3.1. Net Pedersen Current

To characterize the ionospheric Joule heating input, we followed the approach of *Rich et al.* [1987] to combine the currents with ionospheric conductivity under several simplifying assumptions. First, we assumed that the equivalent currents j_{net} represent the net Pedersen current flowing in the ionosphere underneath the spacecraft. As discussed by *Rich et al.* [1987], the equivalence is

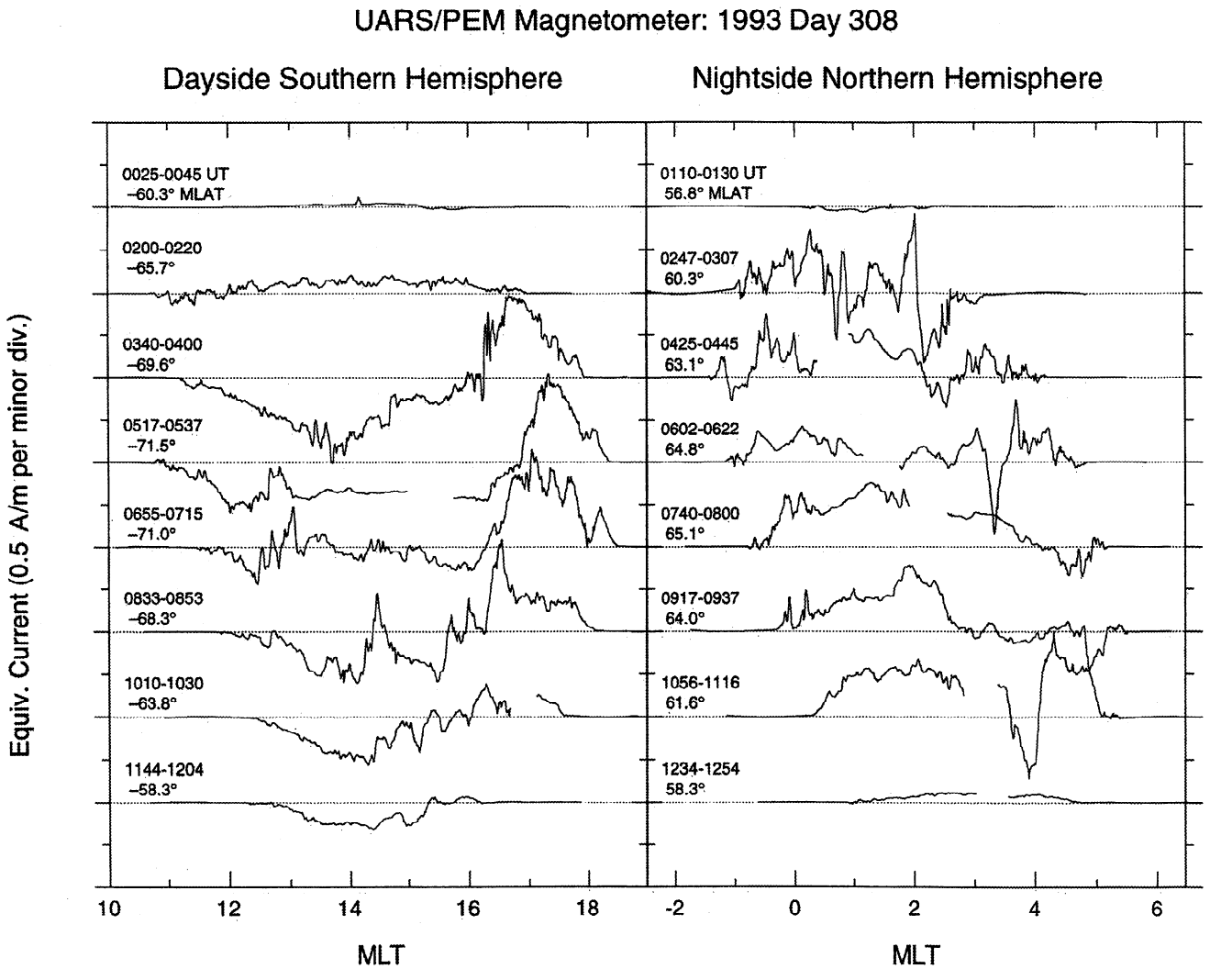

Figure 3. Equivalent currents versus magnetic local time (MLT) for all of the passes on which UARS entered the auroral oval on the November 4, 1993, storm. Dayside (nightside) passes are shown on the left (right). The UT range of data is shown in each panel together with the most poleward magnetic latitude. The polar cap was sampled on the four dayside passes from 0340 UT through 0853 UT and on the three nightside passes from 0740 UT through 1116 UT. Currents were calculated using method 1 described in the text.

exact only for uniform ionospheric conductivity because the Birkeland current is assumed to correspond exactly to the divergence of the Pedersen current. When the conductivity is nonuniform, the divergence of the Hall current will be nonzero and will contribute to the Birkeland currents as well. The equivalence is least reliable in the presence of sharp conductivity gradients. As mentioned above, equating all magnetic perturbations with a current as done here also implies that the Birkeland currents are assumed to be infinite current sheets. For polar orbiting spacecraft, one expects that this is a good approximation [e.g., *Zanetti and Potemra*, 1982] except near noon and midnight. For UARS, however, one must assume that the currents are uniform over the local time sector sampled. Near noon and midnight, where the data suggest the currents are somewhat structured, the latter assumption may not hold. Nonetheless, even when the currents are not sheets, the magnitude of the magnetic perturbations still reflects the net magnitude of the currents fairly well [*Fung and Hoffman*, 1992]. A large discrepancy between methods 1 and 2 indicates that j_{net} does not well represent the Pedersen current.

We also assume that thermospheric winds do not contribute significantly to the Birkeland currents so that the ionospheric electric field and Pedersen currents are parallel. Thermospheric winds have a dynamo effect that contributes to the Birkeland currents [*Lu et al.*, 1995; *Killeen and Roble*, 1984; *Thayer and Vickrey*, 1992; *Deng et al.*, 1993]. Ideally, in our analysis the neutral wind dynamo currents should be removed before estimating the Joule heating. However, the magnetospheric energy is mainly dissipated as ionospheric Joule heating, with only a small fraction, 6%, going into acceleration of thermospheric neutral winds [*Lu et al.*, 1995], so we expect the neutral wind contribution to the currents to be small during the storm main phase. This is supported by *Thayer and Vickrey* [1992] and *Deng et al.* [1993], who found that the neutral wind dynamo makes a significant contribution to the Birkeland currents after major magnetic storms.

3.2. Ionospheric Conductivity

The height-integrated ionospheric Pedersen conductivity due to solar EUV and precipitating electrons was estimated in much the

same way as *Rich et al.* [1987] and as done for input to the AMIE procedure [*Richmond and Kamide*, 1988]. We used the expression of *Brekke and Hall* [1988] for the solar EUV contribution

$$\Sigma_{\text{P-EUV}} = a\cos(\chi) + b\sqrt{\cos(\chi)} \quad \chi < \pi/2 \tag{3a}$$

$$\Sigma_{\text{P-EUV}} = 0 \quad \chi < \pi/2 \tag{3b}$$

where χ is the solar zenith angle, $a = 3.05 \pm 0.85$, $b = 4.06 \pm 0.78$, and $\Sigma_{\text{P-EUV}}$ is in mhos. The average daily solar radio flux, $F10.7$, for the data used to obtain these values was 81, whereas $F10.7$ was 95.7 on November 4, 1993. To adjust for this, we multiplied a and b by the square root of $F10.7$ ratio, $\sqrt{(95.7/81}$ = 1.09 [*Robinson and Vondrak*, 1984].

The conductivity produced by electron precipitation, $\Sigma_{\text{P-elec}}$, was evaluated from the 500 eV to 32 keV electron PEM data, assuming that the fluxes were isotropic using the expression of *Robinson et al.* [1987]

$$\Sigma_{\text{P-elec}} = \frac{40E_{\text{avg}}\sqrt{\varphi_{\text{E}}}}{16 + E_{\text{avg}}^2} \tag{4}$$

where φ_{E} is the electron energy flux in ergs cm^{-2} s^{-1} and E_{avg} is the average electron energy in keV.

The net conductivity is due to the balance of the total production rate against recombination loss. Because the loss rate is proportional to the square of the ion density, the net conductivity Σ_{P} is given by

$$\Sigma_{\text{p}} = \sqrt{\Sigma_{\text{p-EUV}}^2 + \Sigma_{\text{p-elec}}^2} \tag{5}$$

When UARS is sunlit, the satellite acquires a negative potential, and low-energy ions can enter the electron detector where they appear in the high-energy electron channels. Because this occurs against a large solar EUV contribution, this leads to an overestimate of the net Pedersen conductivity by only a fraction of a mho and is ignorable for purposes of estimating Σ_{P}.

3.3. Joule Heating

The Joule heating rate Q_{J} is evaluated from

$$Q_{\text{J1,2}} = j_{\text{net1,2}}^2 / \Sigma_p \tag{6}$$

which is the same as equation (10) of *Rich et al.* [1987]. To compare the profiles of local energy flux from different passes, we integrate over latitude. For a given latitude λ, the dissipation in an interval of azimuth $d\phi$ and latitude $d\lambda$ at 100 km altitude, r = 6470 km, is given by

$$dH_{\text{J}} = Q_{\text{J}}\, r^2 \cos(\lambda) d\lambda d\phi \tag{7}$$

Integrating over latitude gives the heating rate per unit azimuth, $dH_{\text{J}}/d\phi$, which we denote as h_{J}. We performed one such integral for each crossing through the large-scale currents, that is, two for each of the seven auroral zone passes that encountered the polar cap.

3.4. Electron Energy Deposition

To assess the electron energy flux, the background contamination mentioned above cannot be ignored. *Sharber et al.* [this issue] used nightside electron precipitation for which backgrounds are not a problem and extrapolated to a hemispheric energy flux using the statistical pattern of *Hardy et al.* [1985]. To make a pass by pass comparison of electron and Joule heating, however, we need to use electron data from the dayside as well. The background signal appears almost exclusively in the highest four energy channels, 10–30 keV, and is characterized by apparent energy fluxes that increase with increasing energy. Comparison with data from the high-energy particle spectrometer (HEPS) detector, which provides coverage up to MeV energies, confirms that the backgrounds are not the low-energy portion of a real population. Real auroral spectra are well characterized by kappa distributions, $K(\kappa,E_0,E) \propto E(1 + E/\kappa E_0)^{-(k+1)}$ with κ = 4–6 and κE_0 in the 1–10 keV range that have steeply falling energy flux above 10 keV [e.g., *Sharber et al.*, this issue]. The background portion of the signal is then readily identified by comparison with a kappa distribution.

To remove the background contribution, we evaluate a conservatively hard kappa distribution, with $\kappa = 3$ that matches $\varphi(E)$ at 10 keV and best fits the 14-keV channel with κE_0 between 1 and 10 keV. That is, we set $\kappa = 3$ and solve for the E_0 that gives $\varphi(10)$ and $\varphi(14)$. If κE_0 is not between 1 and 10 keV, we change E_0 to match whichever limit is closer. This provides a good estimate of the hardest reasonable spectrum consistent with the 10-keV channel. We then estimate how much of the 30-keV channel is background by comparing K evaluated at 30 keV, $K(\kappa,E_0,30)$, with the observed energy flux at 30 keV, $\varphi(30)$. If the observed flux exceeds the hard kappa distribution, that is, $\varphi(30) > K(\kappa,E_0,30)$, then the difference, $\varphi_{\text{B}}(30) = \varphi(30) - K(\kappa,E_0,30)$, gives the background at 30 keV. Otherwise, we let $\varphi_{\text{B}}(30) = 0$. When the data are dominated by background, the energy flux in the 10-, 14-, and 20-keV channels have the following fixed ratios relative to the flux in the 30-keV channel: 1.01, 0.95, and 0.88, respectively. The backgrounds at 10, 14, and 20 keV are calculated by multiplying $\varphi_{\text{B}}(30)$ by these ratios.

The net electron energy flux is given by

$$Q_{\text{elec}} = \pi \int (\varphi(E) - \varphi_{\text{B}}(E)) dE \tag{8}$$

where the factor of π represents the solid angle of the distribution that precipitates. The energy deposition rate per unit azimuth is evaluated using equation (7) with Q_{elec} to obtain $dH_{\text{elec}}/d\phi$ denoted as h_{elec}.

3.5. Results

Figure 4 shows height-integrated Pedersen conductivity, equivalent currents j_{net1} and j_{net2}, together with Q_{J1}, Q_{J2}, and Q_{elec} for the 0341–0401 UT pass. The EUV conductivity is several mhos on which enhancements up to about 13 mho due to precipitating electrons are superimposed. Method 1 gives somewhat higher dusk currents than method 2. This pass gave the largest discrepancy between the two methods in any of the passes. The Joule heating rates are generally higher than 10 mW/m^2 and reach ~100 mW/m^2 from 0347 UT to 0349 UT in the early afternoon. The discrepancy between j_{net1} and j_{net2} gives differences of tens of mW/m^2 between Q_{J1} and Q_{J2}. From 0345 to 0350 UT, when the spacecraft traversed near 1300 MLT, Q_{elec} is less than 1 mW/m^2. Later, from 0350 to 0355 UT, Q_{elec} is larger, up to 5 mW/m^2, but still much smaller than Q_{J}.

Figure 5 shows corresponding results for the nightside pass that begins at 0917 UT. The good agreement between j_{net1} and j_{net2} and between Q_{J1} and Q_{J2} for this case was more typical. The equivalent currents are less than about 0.5 A/m even though the conductivities are the same or even slightly higher due to electron precipitation than they were for the dayside case. The lower currents result in somewhat lower Q_{J}, ranging from 10 to 30 mW/m^2. By contrast, Q_{elec} is consistently higher for this pass than on the dayside pass,

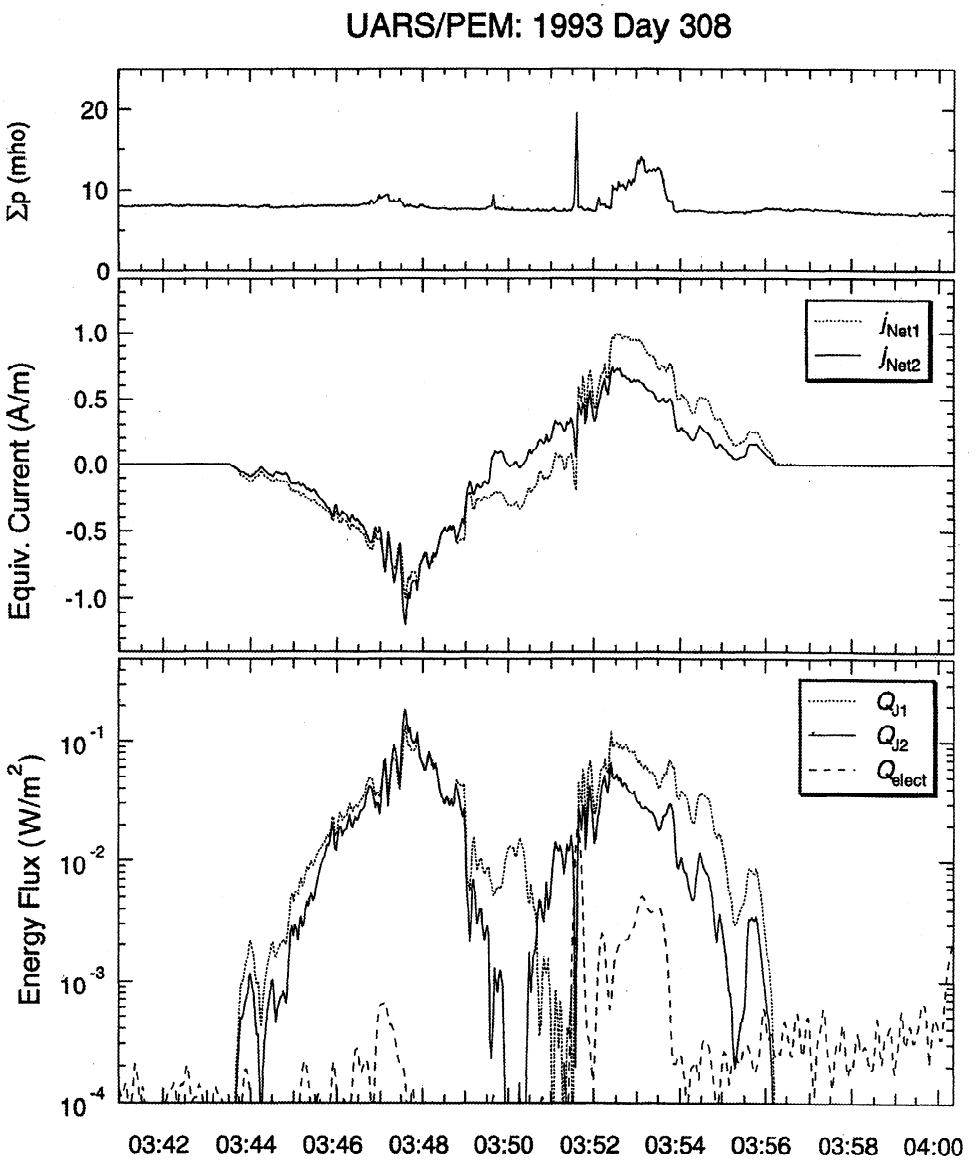

Figure 4. Joule heating estimate for a representative dayside pass, 0341–0401 UT on November 4, 1993. Shown are (top) the total ionospheric Pedersen conductivity, (middle) the equivalent Pedersen currents estimated using both methods described in the text, and (bottom) the Joule Q_J and precipitating electron Q_{elec} energy deposition rates.

with Q_{elec} ranging between 5 and 10 mW/m^2 near midnight, 0922–0928 UT, and up to 10 mW/m^2 near dawn.

Figure 6 shows the results for h_J and h_{elec} for the 14 auroral traversals plotted against MLT and expressed as gigawatts per MLT hour, GW/h. The horizontal error bars give the MLT range of the corresponding latitude integral, and for h_J the vertical error bars indicate the range of values from methods 1 and 2. The h_J in the late afternoon tend to be over 10 GW/h, higher than at other local times, where h_J is typically in the range 5–10 GW/h, with the exception of one pass near midnight. The variation of h_{elec} with MLT is much stronger, displaying a deep minimum near noon below 0.6 GW/h and in two cases lower than 0.1 GW/h. This deep minimum near noon and a nightside maximum are consistent with the statistical results of *Hardy et al.* [1985] and *Fuller-Rowell and Evans* [1987]. The highest h_{elec} occurs near midnight, where two passes gave $h_{elec} \approx 6$ GW/h. It is clear that the local time variations in h_J and h_{elec} lead to a strong variation in their ratio with local time.

Table 1 summarizes the Joule heating rate calculation results. The table gives h_J, the average conductivity, and average and maximum equivalent current magnitude for each pass. Comparing the h_J for methods 1 and 2 suggests that the net heating rates are uncertain by at most a factor of 1.5–2 and generally less. Table 2 compares h_{elec} with h_J and gives the averages, the ratios h_J/h_{elec}, and the totals $h_J + h_{elec}$ in each local time sector. The highest h_J occurred in the late afternoon; h_J in the other sectors were a factor of 2–3 lower. By contrast, h_{elec} maximizes at midnight, is a factor of 2–3 lower at dawn and late afternoon, and is a factor of roughly 20 lower in the early afternoon. These nearly opposite variations in h_J and h_{elec} combine to produce a large, 20- to 40-fold, variation in h_J/h_{elec}. Near midnight, h_J/h_{elec} is about 2 and rises slightly toward dawn to about 3. In the late afternoon, h_J/h_{elec} is 10–15, and

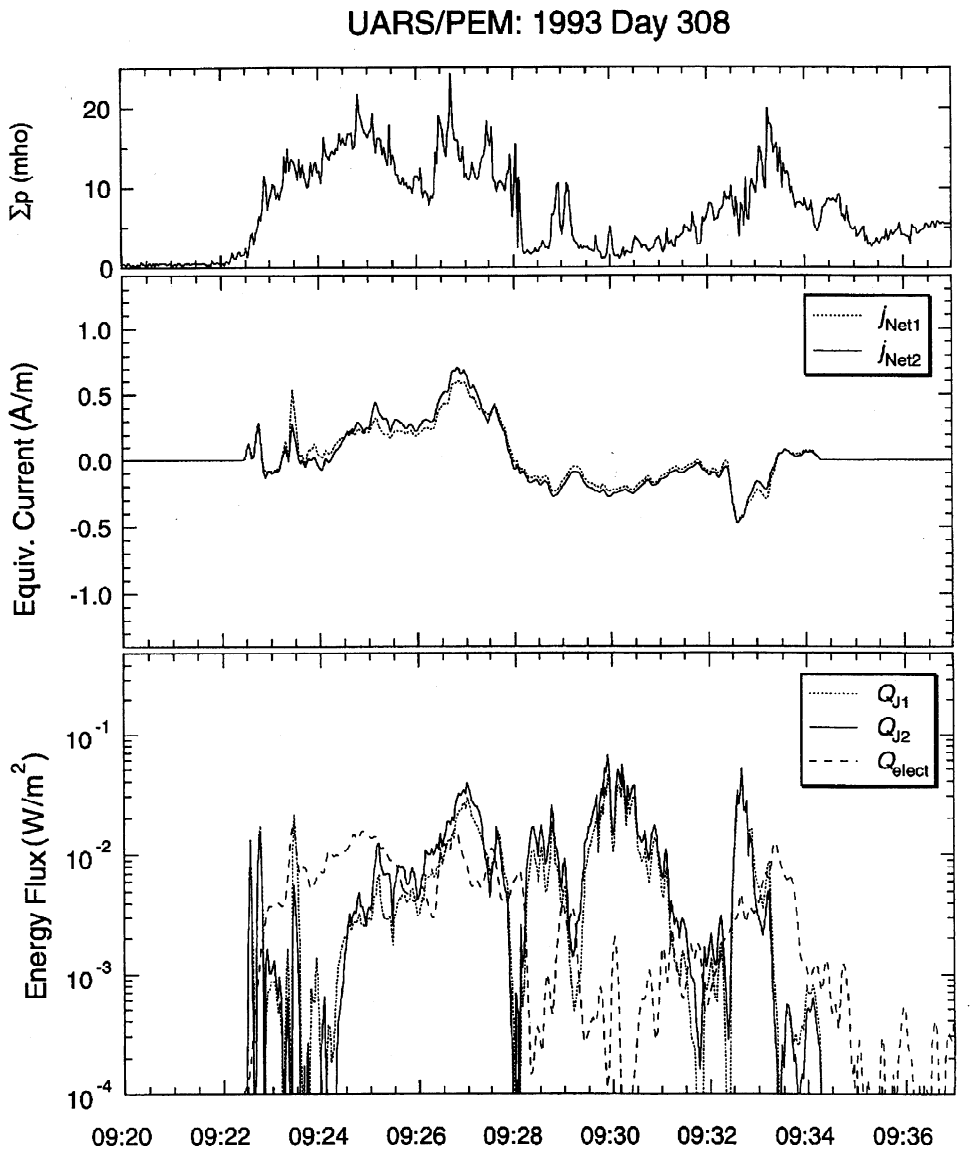

Figure 5. Joule heating estimate for a representative nightside pass, 0920–0937 UT on November 4, 1993, in the same format as Figure 4.

just postnoon h_J/h_{elec} is often near 100. The total energy deposition varies by less than a factor of 4 with local time and maximizes in the late afternoon where Joule heating dominates. Near midnight the total heating is about half the value in the late afternoon.

To estimate the hemispherical heating rates, denoted H_J and H_{elec}, we treat each sector as representative of 25% of the auroral oval. These values then give hemispherical heating rates of $H_J \approx$ 290 GW and $H_{elec} \approx$ 50 GW so that $H_J/H_{elec} \approx 4$ and $H_J + H_{elec}$ = 340 GW during the storm main phase. In making these averages, we implicitly assume that the UARS passes represent the average storm main phase conditions.

4. Discussion and Conclusions

There are four principal points to be drawn from the UARS observations: (1) The hemispheric heating rates obtained here are in reasonable agreement with AMIE results; (2) the auroral currents expand equatorward significantly for this minimum $Dst = -116$ nT storm; (3) Joule heating dominates the energy input and is largest in the afternoon; and (4) the relative contributions of Joule and precipitation heating vary greatly with local time.

Comparison with the AMIE results for this storm indicate reasonable agreement in overall heating rates. The AMIE results for the main phase of this storm [*Knipp et al.*, this issue], yield hemispherically averaged values of $H_J \approx$ 200 GW and $H_{elec} \approx$ 80 GW. These values are averages, however, and the AMIE results indicate that both the Joule heating and electron precipitation varied considerably during the storm main phase. To make a valid comparison, we should consider the AMIE results for the times of the relevant UARS passes. Since the electron energy deposition is dominated by the nightside passes, we should take the AMIE runs corresponding to these three passes to compare H_{elec}. The averages of the AMIE runs at 0750, 0900–0945, and 1130 UT give an electron heating rate of 68 GW, ranging from 44 GW to 114 GW (B. Emery and D. Knipp, private communication, 1997). Given that UARS did not traverse the premidnight region, where a significant

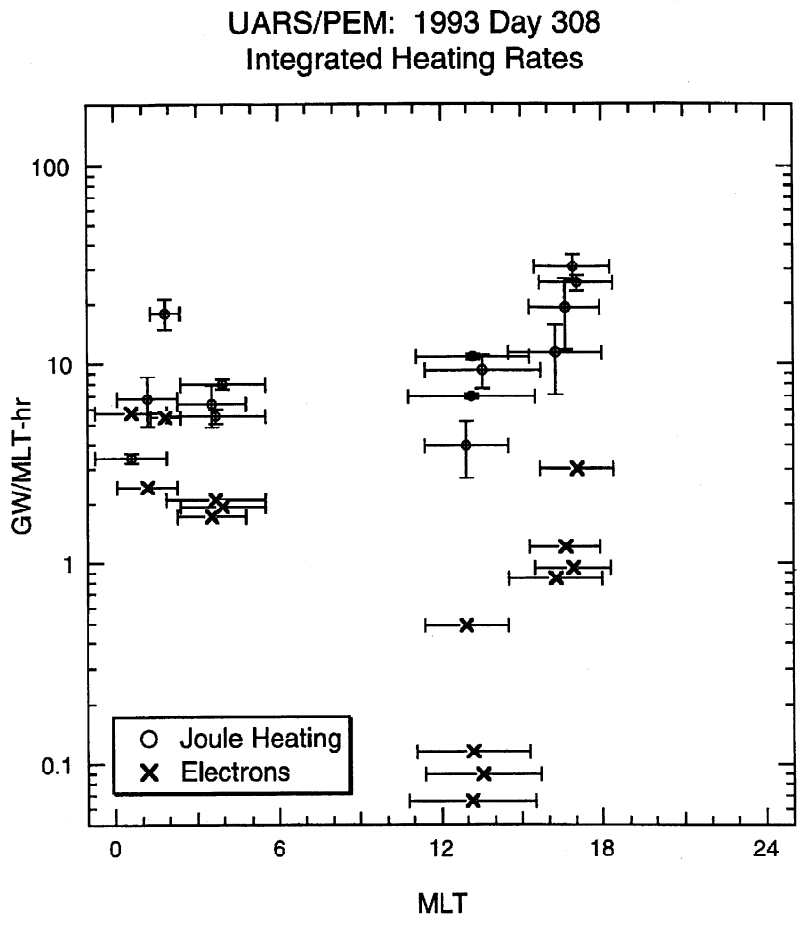

Figure 6. Plot of Joule heating rate h_J and electron precipitation energy flux h_{elec} per unit local time in GW/h plotted against local time for the 14 UARS traversals of the large-scale currents during the November 4, 1993, storm. Vertical error bars for h_J indicate the range between methods 1 and 2 for estimating the net Pedersen currents. The symbols show the average value. Horizontal error bars indicate the range of MLT for the traversal, and the point shows the average MLT.

fraction of substorm precipitation can occur, it is not surprising that the UARS electron heating rate presented here falls in the lower range of the AMIE results. The UARS Joule heating rates are dominated by the dusk sector which was sampled on the 0341, 0520, 0658, and 0832 UT passes. Taking the AMIE runs for 0345, 0530, 0700, and 0840 UT (B. Emery and D. Knipp, private communication, 1997) gives an average hemispherical Joule heating rate from AMIE of 264 GW. This value is known to be about 8% low due to a systematic underestimate of the electric field in AMIE [*Knipp et al.*, this issue], and if we include an 8% correction we get an AMIE value of H_J = 285 GW, in good agreement with the UARS result. Thus comparing the AMIE results for the relevant times shows that the UARS observations and AMIE results are in reasonable agreement if one accounts for dynamic variability during the main phase.

That the auroral oval and the large-scale currents expand equatorward with increasing activity is well documented [*Iijima and Potemra*, 1978; *Hardy et al.*, 1985; *Foster et al.*, 1989], but there has been debate concerning how far equatorward the electrojets move during storms. Analyses of the variation of the *AE* index with increasing storm severity, measured with *Dst*, have attributed the leveling off of *AE* for storms with $Dst < -150$ nT to a saturation of the polar cap potential [*Reiff et al.*, 1981; *Wygant et al.*, 1983]. It has been shown, however, that during great storms the Birkeland currents expand equatorward of the stations used to compile *AE* [*Fujii et al.*, 1992; *Feldstein et al.*, 1997]. The observations presented here show that dramatic equatorward expansions of the Birkeland and ionospheric current systems occur not just for intense storms, $Dst < -150$, but for more moderate storms as well. For this storm, the auroral electrojets were displaced to 60° magnetic latitude, approximately 10° equatorward of their nominal moderate activity latitudes. It is important to study whether the equatorward expansion occurs generally for large storms because this could have important implications for storm analyses based primarily on high-latitude ground stations.

It is customary to evaluate the relative contributions of particle and Joule heating in the ionosphere in terms of the ratio of their hemispheric dissipation rates, H_J/H_{elec} [e.g., *Ahn et al.*, 1983]. Using statistical models of ionospheric conductivity to infer particle precipitation input and an extensive ground magnetometer network to infer the Pedersen currents, *Ahn et al.* [1983] estimated H_J/H_{elec} to be close to 3. During this storm, H_J/H_{elec} was over 4. The hemispheric dissipation ratio found here is a little higher than expected from statistical correlations. Analysis of ion drift measurements has been used to infer the H_J as well; *Foster et al.*[1983] found that H_J increases linearly with *Kp* from 25 GW to 85 GW

Table 1. Net Pedersen Currents j_{Net}, Average Pedersen Conductivities Σ_P, and Integrated Joule Heating Rates h_J, for the Seven UARS Auroral Zone Passes That Crossed Into the Polar Cap During the November 4, 1993, Storm

Pass, UT	Magnetic Local Time	Average $\|j_{net}\|$, A/m		Maximum $\|j_{net}\|$, A/m		Average Σ_p, mhos	h_J, GW/h		
		Method 1	Method 2	Method 1	Method 2		Method 1	Method 2	Average
0741	1.9	0.33	0.39	0.65	0.78	8.4	14.8	20.0	17.4
0920	0.6	0.23	0.26	0.60	0.70	12.4	3.2	3.6	3.4
1100	1.2	0.29	0.41	0.56	0.67	9.8	5.0	8.7	6.8
0741	4.0	0.14	0.17	0.37	0.38	4.3	7.5	8.3	7.9
0920	3.7	0.13	0.16	0.47	0.48	5.8	5.1	6.0	5.5
1100	3.6	0.32	0.28	1.01	0.80	10.2	7.8	4.8	6.3
0341	13.2	0.39	0.35	1.01	1.20	7.3	10.3	9.8	10.1
0520	13.2	0.28	0.30	0.60	0.70	7.4	6.3	6.8	6.6
0658	13.6	0.45	0.38	1.14	0.98	7.9	11.7	8.1	9.9
0832	13.0	0.29	0.20	0.75	0.72	8.7	5.6	3.0	4.3
0341	16.6	0.43	0.30	0.99	0.74	9.6	30.3	13.2	21.7
0520	16.9	0.45	0.38	1.14	0.98	9.4	42.4	31.1	36.7
0658	17.1	0.46	0.48	0.96	0.95	10.8	26.8	32.2	29.5
0832	16.3	0.35	0.21	1.08	0.70	9.4	19.7	8.9	14.3

The data are grouped into four MLT ranges: midnight, predawn, noon, and late afternoon. Within each group the data are ordered chronologically. Results for j_{net} and h_J are given for both analysis methods (see text for details). Note that one cannot estimate h_J from the average j_{net} and Σ_P because the correlation between j_{net} and Σ_P is generally poor and highly variable from pass to pass.

as *Kp* changes from 1 to 4. The highest value of *Kp* on November 4, 1993, was 7⁻. The linear relation to *Kp* of *Foster et al.* [1983] predicts H_J = 140 GW, which is less than half the 290 GW estimated here. On the basis of empirical relations between H_J, H_{elec}, and activity indices, it has been suggested that H_J/H_{elec} decreases below 1 during major storms [*Monreal Mac-Mahon and Gonzalez*, 1997]. For this storm we find that H_J/H_{elec} is higher than nominal values, not lower. Since *Monreal-MacMahon and Gonzalez* [1997] only studied storms with *Dst* < –240 nT, it is possible that the decrease in H_J/H_{elec} they inferred only occurs for the most intense storms.

The local time distribution of Joule heating obtained for this storm is similar to the average pattern. The local time variation of electron precipitation has been studied extensively [*Hardy et al.*, 1985; *Fuller-Rowell and Evans*, 1987], and the deep minimum just postnoon observed for this storm is present on average for high *Kp* conditions. Statistical studies have characterized the local time variation of Joule heating as well [*Banks et al.*, 1981; *Foster et al.*,

Table 2. Electron Precipitation Energy Flux h_{elec}, the Average Joule Heating Rate h_J, h_J/h_{elec}, and $h_{elec} + h_J$

Pass, UT	Magnetic Local Time	h_{elec}, GW/h	h_J, GW/h	h_J/h_{elec}	$h_{elec} + h_J$
0741	1.9	5.4	17.4	3.2	23.8
0920	0.6	5.7	3.4	0.60	9.1
1100	1.2	2.4	6.8	2.8	9.2
Average		4.5	9.2 ± 4.2	2.2 (2.0)	14.0
0741	4.0	1.94	7.9	4.1	9.8
0920	3.7	2.1	5.5	2.6	7.6
1100	3.6	1.73	6.3	3.6	8.0
Average		1.92	6.6 ± 0.7	3.4 (3.4)	8.5
0341	13.2	0.12	10.1	84	10.2
0520	13.2	0.07	6.6	94	6.7
0658	13.6	0.09	9.9	110	10.0
0832	13.0	0.49	4.3	8.8	4.8
Average		0.19	7.7 ± 1.4	74 (41)	7.9
0341	16.6	1.20	21.7	18.1	22.9
0520	16.9	0.94	36.7	39.0	37.6
0658	17.1	3.0	29.5	9.8	32.5
0832	16.3	0.84	14.3	17.0	15.1
Average		1.5	25.6 ± 4.8	21.0 (17.1)	27.0

As in Table 1, the data are organized by magnetic local time. The average values for each local time sector are also given. The values in parentheses are the ratios of the average h_J and h_{elec} values.

1983; *Rich et al.*, 1991]. *Foster et al.* [1983] found a fairly uniform heating with local time, with some tendency for the heating to maximize in the dawn and dusk regions, consistent with the present observations. Synoptic radar observations have also been used to characterize the local time variation of Joule heating [*Banks et al.*, 1981] from which a fair degree of structure is apparent, but comparable heating rates were observed at all local times. Banks et al. concluded that any systematic local time variations were smaller than changes with magnetic activity, which often yielded $Q_J > 50$ mW/m^2. *Rich et al.* [1991] used 2 years of DMSP magnetic field and particle data during solar minimum to evaluate the distribution of Joule heating and its dependence on season, IMF sector structure, and geomagnetic activity. They found that Joule heating is generally higher on the dayside and displays local maxima near dawn and dusk as well. In summer the dayside maximum is largest, whereas in winter the dayside, dawn, and dusk maxima are comparable.

The variation of h_J/h_{elec} with local time has not been studied previously. By comparing field-aligned current and precipitating electron observations we have shown that the diurnal variation in h_J/h_{elec} is larger than a factor of 10. This is consistent with previous statistical studies that considered Joule heating and electron precipitation separately [*Foster et al.*, 1983; *Rich et al.*, 1991; *Hardy et al.*, 1985; *Fuller-Rowell and Evans*, 1987]. The effect is due primarily to the deep minimum in h_{elec} near noon because although h_J maximizes on the dayside, its local time variation is smaller. The opposite dependencies of h_{elec} and h_J with local time probably arise because in sunlit regions one can find large Birkeland and Pedersen currents without large particle precipitation fluxes, whereas the dark ionosphere appears to require significant particle precipitation to support the nightside currents [e.g., *Newell et al.*, 1996]. This would be consistent with a view of the nightside generator as a current generator [e.g., *Rich et al.*, 1991]. With regard to the dayside heating rates, the present results would be obtained whether the dayside source were a current or voltage source because the solar EUV provides a large background conductivity at the latitudes of the highly expanded oval. Thus, in any case, the particle precipitation is most intense at night, while the large-scale currents are most intense on the dayside. The approximate antiphase local time variations of h_J and h_{elec} mean that the total energy deposition rate is more uniform in local time than either alone.

Acknowledgments The PEM instrument is supported under contract NAS5-27753 between NASA and Southwest Research Institute (SwRI). Support for work at The Johns Hopkins University Applied Physics Laboratory was provided by NSF and ONR and under subcontract with SwRI.

The Editor thanks Barbara Emery and John Foster for their assistance in evaluating this paper.

References

Ahn, B.-H., S.-I. Akasofu, and Y. Kamide, The Joule heat production rate and the particle energy injection rate as a function of the geomagnetic indices AE and AL, *J. Geophys. Res.*, *88*, 6275–6287, 1983.

Anderson, B. J., T. A. Potemra, P. F. Bythrow, L. J. Zanetti, D. B. Holland, and J. D. Winningham, Auroral currents during the magnetic storm of November 8 and 9, 1991: Observations from the Upper Atmosphere Research Satellite particle environment monitor, *Geophys. Res. Lett.*, *20*, 1327–1330, 1993.

Banks, P. M., J. C. Foster, and J. R. Doupnik, Chanika radar observation relating to the latitudinal and local time variations of Joule heating, *J. Geophys. Res.*, *86*, 6869–6878, 1981.

Brekke, A., and C. Hall, Auroral ionospheric quiet summer time conductances, *Ann. Geophys.*, *6*, 361–376, 1988.

Cooper, M. L., C. R. Clauer, B. A. Emery, A. D. Richmond, and J. D. Winningham, A storm time assimilative mapping of ionospheric electrodynamics analysis for the severe geomagnetic storm of November 8–9, 1991, *J. Geophys. Res.*, *100*, 19,329–19,342, 1995.

Deng, W., T. L. Killeen, A. G. Burns, R. G. Roble, J. A. Slavin, and L. E. Wharton, The effects of neutral inertia on ionospheric currents in the high-latitude thermosphere following a geomagnetic storm, *J. Geophys. Res.*, *98*, 7775–7790, 1993.

Feldstein, Y. I., A. Grafe, L. I. Gromova, and V. A. Popov, Auroral electrojets during geomagnetic storms, *J. Geophys. Res.*, *102*, 14,223–14,235, 1997.

Foster, J. C., J.-P. St.-Maurice, and V. J. Abreu, Joule heating at high latitudes, *J. Geophys. Res.*, *88*, 4885–4896, 1983.

Foster, J. C., T. Fuller-Rowell, and D. S. Evans, Quantitative patterns of large-scale field-aligned currents in the auroral ionosphere, *J. Geophys. Res.*, *94*, 2555–2564, 1989.

Fuller-Rowell, T. J., and D. S. Evans, Height-integrated Pedersen and Hall conductivity patterns inferred from the TIROS-NOAA satellite data, *J. Geophys. Res.*, *92*, 7606–7618, 1987.

Fujii, R., H. Fukunishi, S. Kokubun, M. Sugiura, F. Tohyama, H. Hayakawa, K. Tsuruda, and T. Okada, Field-aligned current signatures during the March 13–14, 1989, great magnetic storm, *J. Geophys. Res.*, *97*, 10,703–10,715, 1992.

Fung, S. F., and R. A. Hoffman, Finite geometry effects of field-aligned currents, *J. Geophys. Res.*, *97*, 8569–8579, 1992.

Hardy, D. A., M. S. Gussenhoven, and E. Holeman, A statistical model of auroral electron precipitation, *J. Geophys. Res.*, *90*, 4229–4248, 1985.

Iijima, T., and T. A. Potemra, The amplitude distribution of field-aligned currents at northern high latitudes observed by Triad, *J. Geophys. Res.*, *81*, 2165–2174, 1976.

Iijima, T., and T. A. Potemra, Large-scale characteristics of field-aligned currents associated with substorms, *J. Geophys. Res.*, *83*, 599–615, 1978.

Killeen, T. L., and R. G. Roble, An analysis of the high-latitude thermospheric wind pattern calculated by a thermospheric general circulation model, 1., Momentum forcing, *J. Geophys. Res.*, *89*, 7509–7522, 1984.

Knipp, D. J., et al., Ionospheric convection response to slow, strong variations in a northward interplanetary magnetic field: A case study for January 14, 1988, *J. Geophys. Res.*, *98*, 19,273–19,292, 1993.

Knipp, D. J., et al., An overview of the early November 1993 geomagnetic storm, *J. Geophys. Res.*, this issue.

Lu, G., D. Richmond, B. A. Emery, and R. G. Roble, Magnetosphere-ionosphere-thermosphere coupling: Effect of neutral winds on energy transfer and field-aligned current, *J. Geophys. Res.*, *100*, 19,643–19,659, 1995.

Lu, G., et al., High-latitude ionospheric electrodynamics as determined by the assimilative mapping of ionospheric electrodynamics procedure for the conjunctive SUNDIAL/ATLAS 1/GEM period of March 28–29, 1992, *J. Geophys. Res.*, *101*, 26,697–26,718, 1996.

Monreal Mac-Mahon, R., and W. D. Gonzalez, Energetics during the main phase of geomagnetic superstorms, *J. Geophys. Res.*, *102*, 14,199–14,207, 1997.

Newell, P. T., C.-I. Meng, and K. M. Lyons, Suppression of discrete aurorae by sunlight, *Nature*, *381*, 766–767, 1996.

Potemra, T. A., Sources of large-scale Birkeland currents, in *Physical Signatures of Magnetospheric Boundary Layer Processes*, edited by J. A. Holtet and A. Egeland, pp. 3–27, Kluwer Acad., Norwell, Mass., 1994.

Reiff, P. H., R. W. Spiro, and T. W. Hill, Dependence of polar cap potential drop on interplanetary parameters, *J. Geophys. Res.*, *86*, 7639–7648, 1981.

Rich, F. J., M. S. Gussenhoven, and M. E. Greenspan, Using simultaneous particle and field observations on a low altitude satellite to estimate Joule heat energy flow into the high latitude ionosphere, *Ann. Geophys.*, *5A*, 527–534, 1987.

Rich, F. J., D. A. Hardy, R. H. Redus, and M. S. Gussenhoven, Northward IMF and patterns of high-latitude precipitation and field-aligned currents: the February 1986 storm, *J. Geophys. Res.*, *95*, 7893–7913, 1990.

Rich, F. J., M. S. Gussenhoven, D. A. Hardy, and E. Holeman, Average height-integrated Joule heating rates and magnetic deflection vectors due to field-aligned currents during sunspot minimum, *J. Atmos. Sol. Terr. Phys.*, *53*, 293–308, 1991.

Richmond, A. D., and Y. Kamide, Mapping electrodynamic features of the high-latitude ionosphere from localized observations: Technique, *J. Geophys. Res.*, *93*, 5741–5759, 1988.

Robinson, R. M., and R. R. Vondrak, Measurements of *E* region ionization and conductivity produced by solar illumination at high latitudes, *J. Geophys. Res.*, *89*, 3951–3956, 1984.

Robinson, R. M., R. R. Vondrak, K. Miller, T. Dabbs, and D. Hardy, On calculating ionospheric conductances from the flux and energy of precipitating electrons, *J. Geophys. Res.*, *92*, 2565–2569, 1987.

Sharber, J. R., R. A. Frahm, R. Link, G. Crowley, J. D. Winningham, E. E. Gaines, R. W. Nightingale, R. L. Chenette, B. J. Anderson, and C. A. Gurgiolo, UARS particle environment monitor observations during the November 1993 storm: Auroral morphology, spectral characterization, and energy deposition, *J. Geophys. Res.*, this issue.

Thayer, J. P., and J. F. Vickrey, On the contribution of the thermospheric neutral wind to high-latitude energetics, *Geophys. Res. Lett.*, *19*, 265–268, 1992.

Winningham, J. D., et al., The UARS particle environment monitor, *J. Geophys. Res.*, *98*, 10,649–10,666, 1993.

Wygant, J. R., R. B. Torbert, and F. S. Mozer, Comparison of S3-3 polar cap potential drops with the interplanetary magnetic field and models of magnetopause reconnection, *J. Geophys. Res.*, *88*, 5727–5735, 1983.

Zanetti, L. J., and T. A. Potemra, Correlated Birkeland current signatures from the Triad and MAGSAT magnetic field data, *Geophys. Res. Lett.*, *9*, 349–352, 1982.

B. J. Anderson and T. A. Potemra, Applied Physics Laboratory, The Johns Hopkins University, 11100 Johns Hopkins Road, Laurel, MD 20723-6099. (e-mail: brian.anderson@jhuapl.edu)

R. A. Frahm, J. R. Sharber, and J. D. Winningham, Southwest Research Institute, 6220 Culebra Road, San Antonio, TX 78228. (e-mail: jsharber@swri.edu)

J. B. Gary, Information Resource Department, University of Texas at Dallas, 2601 N. Floyd Road, Richardson, TX 75083-0688.

(Received November 18, 1997; revised March 17, 1998; accepted April 3, 1998.)